

Impurity transport in temperature gradient driven turbulence

A. Skyman
H. Nordman
P. Strand

*Euratom-VR Association, Department of Earth and Space Sciences,
Chalmers University of Technology,
SE-412 96 Göteborg, Sweden*

Abstract

In the present paper the transport of impurities by TE and ITG mode driven turbulence is studied. Results obtained using a multi-fluid model are compared with quasilinear (QL) and nonlinear (NL) gyrokinetic results acquired using the code GENE. The main part of the work is devoted to a comparison between TE mode and ITG mode dominated turbulence, with regard to the impurity peaking factor obtained for zero impurity flux. In particular, the scaling of the peaking factor with impurity charge Z and with the driving background gradients is investigated.

For the scaling with the impurity charge Z , the TE and ITG mode dominated cases show different scalings. For ITG mode driven impurity transport, the peaking factor is at a minimum for low Z impurities. For larger Z values, the peaking factor is found to increase followed by a saturation at a level much below neoclassical predictions. The models considered (fluid and QL GENE) give similar results, in line with a previous study based on JET data¹ including NL GENE simulations. For TE mode transport, on the other hand, a rather flat Z scaling is obtained using fluid and NL GENE simulations. Hence, TE mode turbulence results in larger peaking factors than ITG mode turbulence for low Z values and vice versa for large Z impurities.

The difference in the Z scalings are discussed in terms of theoretical expectations, and interpretation of the data is found based on the sign and Z scalings of the different terms contributing to the convective impurity flux.

The scaling with the driving background gradients is in most cases found to be weak. The exception is the scaling with the density gradient for low Z values in ITG driven turbulence, where a strong rising trend in the peaking factor with ∇n_e is observed.

It is found that the convective pinch is generally inward for both TE and ITG mode driven transport for all scalings.

1 Introduction

The transport properties of impurities is of high relevance for the performance and optimisation of magnetic fusion devices. For instance, the possible accumulation of He ash in the core of the reactor plasma will serve to dilute the fuel, thus lowering fusion power. Heavier impurity species, originating from the plasma-facing surfaces, may also accumulate in the core, and wall-impurities of relatively low density may lead to unacceptable energy losses in the form of radiation. In an operational power plant, both impurities of low and high charge numbers will be present.

In the confinement zone of tokamaks, the transport is usually dominated by turbulence. The Trapped Electron (TE) mode and the Ion Temperature Gradient (ITG^{a)}) mode are expected to be the main contributors. Turbulent impurity transport has been investigated in a number of theoretical^{1–22} and experimental^{1,23–27} papers. The main theoretical effort has hitherto been devoted to the study of ITG mode driven transport. For the more reactor relevant regimes, however, where α -particle heating dominates, as will be the case in the ITER device, or in

^{a)}also commonly referred to as the η_i mode

electron cyclotron resonance heated plasmas, TE mode driven impurity transport will likely be important. In tokamak experiments the impurity transport is usually dominated by turbulence, resulting in impurity peaking factors well below the neoclassical predictions.^{1,27,28}

In the present study, transport of impurities driven by the TE mode is compared to and contrasted with ITG mode dominated impurity transport. The different modes are studied using fluid and gyrokinetic models. Quasilinear (QL) and nonlinear (NL) results obtained from the GENE code^{29–31} are compared with fluid results³² for both TE and ITG mode dominated turbulence, and compared to results from a previous study focused on the ITG mode.¹ The Weiland multi-fluid model³² is employed for the dual purposes of acquiring comparable simulation data and interpreting the results.

The impurity diffusivity (D_Z) and convective velocity (V_Z) are estimated from simulation data, and from these the zero-flux peaking factor (PF) is derived. This quantity expresses the impurity density gradient at which the convective and diffusive transport of impurities are exactly balanced. The sign of PF is of special interest, as it determines whether the impurities are subject to an inward ($PF > 0$) or outward ($PF < 0$) pinch. Scalings of peaking factors with impurity charge (Z), electron and ion temperature gradients ($\nabla T_{e,i}$), and electron density gradient (∇n_e), are studied, giving particular attention to ∇T_e driven TE mode impurity transport.

The remainder of the paper is structured as follows: first the transport models are introduced, beginning with the fluid model employed (section 2.1) where the focus is on the impurity dynamics and special attention is given to the concept of the peaking factor (section 2.1.1). This is followed by a brief introduction of the gyrokinetic model and the GENE code (section 2.2). After this, the main results are covered, including discussion and interpretation of the acquired results. The final section of the paper is a summary of the main conclusions to be drawn (section 5).

2 Transport models

To arrive at a set of equations describing the impurity transport that are both meaningful and solvable, some approximations are necessary. The advances in high performance computing have allowed fusion modellers to move from fluid descriptions of the plasma to kinetic descriptions as the basis for turbulence modelling, however, the underlying physics are easier to grasp from fluid models.

In kinetic theory the plasma is described through distribution functions of velocity and position for each of the included plasma species. Hence, kinetic equations are inherently six-dimensional, however, in magnetically confined fusion plasmas the confined particles are generally constrained to tight orbits along field lines. This motivates averaging over the gyration, reducing the problem to five-dimensional gyrokinetic equations.^{33–36} Since the equations governing the evolution of distributions are all coupled, the resulting decrease in numerical complexity is considerable.

Fluid theory, on the other hand, is derived by taking the moments of the kinetic equations to some order, making them tractable by finding an appropriate closure.^{32,37} In addition to making the workings of the plasma more accessible, by reintroducing familiar physical concepts such as pressure and density, fluid models are also several orders of magnitude more computationally efficient.

In the present study, a simple s- α geometry is assumed for the simulation domains. The effects of different tokamak geometries on drift wave turbulence have been studied for fluid theory, and are known to be rather small.^{38,39} The potential effects of using a more realistic geometry on impurity transport are left for further studies.

2.1 Fluid theory

The Weiland multi-fluid model³² consists of coupled sets of equations for each constituent particle species: main ions, electrons and impurities.^{1,2,13,14,40} Neglecting finite Larmor radius effects, the impurity equations of continuity, parallel motion and energy take the form of Eq. (1)–(3).

$$(\tilde{\omega} + \tau_Z^*) \tilde{n}_Z - \left(\frac{R}{2L_{n_Z}} - \lambda \right) \tilde{\phi} + \tau_Z^* \tilde{T}_Z - \frac{k_{\parallel} \delta v_{\parallel Z}}{\omega_{De}} = 0 \quad (1)$$

$$(\tilde{\omega} - 2\tau_Z^*) \frac{k_{\parallel} \delta v_{\parallel Z}}{\omega_{De}} = \frac{Z}{A_Z q_*^2} \tilde{\phi} + \frac{\tau_Z}{A_Z q_*^2} (\tilde{n}_Z + \tilde{T}_Z) \quad (2)$$

$$\left(\tilde{\omega} + \frac{5}{3} \tau_Z^* \right) \tilde{T}_Z - \left(\frac{R}{2L_{T_Z}} - \frac{1}{3} \frac{R}{L_{n_Z}} \right) \tilde{\phi} - \frac{2}{3} \tilde{\omega} \tilde{n}_Z = 0 \quad (3)$$

In Eq. (1)–(3), $\tilde{n}_Z = \delta n_Z / n_Z$ is the density, $\tilde{\phi} = e\phi / T_e$ the electrostatic potential, $\tilde{T}_Z = \delta T_Z / T_e$ the temperature and $\delta v_{\parallel Z}$ the parallel velocity. The normalised eigenvalue and wave vector of the eigenmodes are $\tilde{\omega} = \tilde{\omega}_r + i\gamma$ and $\mathbf{k} = k_{\parallel} \hat{\mathbf{z}} + \mathbf{k}_{\perp}$, \sim denoting normalisation with respect to the electron magnetic drift frequency ω_{De} . The normalised scale lengths can be assumed to be constant for the flux tube domain considered, and are defined as $\frac{R}{L_{X_j}} = -\frac{R}{X_j} \frac{\partial X_j}{\partial r}$, where R is the major radius of the tokamak, $X_j = n_j, T_j$ for species j . The other parameters are defined as follows: $\tau_Z^* = \lambda T_Z / Z T_e$ with $\lambda = \cos \theta + s \theta \sin \theta$ for the poloidal angle θ , $\tau_Z = T_Z / T_e$, $A_Z = m_Z / m_i \approx 2Z$ is the impurity mass number, Z is the impurity charge. Further, s is the magnetic shear and $q^* = 2qk_{\theta} \rho_s$, where q is the safety factor, $\rho_s = c_s / \Omega_{ci}$ is the ion sound scale with the ion sound speed $c_s = \sqrt{T_e / m_i}$ and the ion cyclotron frequency $\Omega_{ci} = eB / m_i$. Effects of curvature enter the equations through the magnetic drift, defined as $\omega_{DZ} = \omega_{DZ}^{\theta=0} \lambda(\theta)$, which originates from the compression of the $\mathbf{E} \times \mathbf{B}$ drift velocity, the diamagnetic drift velocity and the diamagnetic heat flow. Curvature effects from the stress tensor enter as $2\tau_Z^*$ at the left hand side of Eq. (2).

Combining Eq. (1)–(3), while neglecting pressure perturbations in Eq. (2) for simplicity, the relation of the electrostatic potential $\tilde{\phi}$ and impurity density \tilde{n}_Z becomes:

$$\tilde{n}_Z = \left[\tilde{\omega} \left(\frac{R}{2L_{n_Z}} - \lambda \right) - \tau_Z^* \left(\frac{R}{2L_{T_Z}} - \frac{7}{3} \frac{R}{2L_{n_Z}} + \frac{5\lambda}{3} \right) + \frac{Z}{A_Z q_*^2} \left(\frac{\tilde{\omega} + 5\tau_Z^*/3}{\tilde{\omega} - 2\tau_Z^*} \right) \right] \frac{\tilde{\phi}}{N}, \quad (4)$$

where

$$N = \tilde{\omega}^2 + \frac{10\tau_Z^*}{3} \tilde{\omega} + \frac{5\tau_Z^{*2}}{3}. \quad (5)$$

The main ion and electron response is calculated from the corresponding fluid equations for ions and trapped electrons. The electron response is given by a trapped and a free part such that $\frac{\delta n_e}{n_e} = f_t \frac{\delta n_{et}}{n_{et}} + (1 - f_t) \frac{e\phi}{T_e}$, i.e. the free electrons are assumed to be adiabatic and thus to follow the Boltzmann distribution: $\delta n_{ef} / n_{ef} = e\phi / T_e$.

The equations are closed by the assumption of quasineutrality:

$$\frac{\delta n_e}{n_e} = (1 - Zf_Z) \frac{\delta n_i}{n_i} + Zf_Z \frac{\delta n_Z}{n_Z}, \quad (6)$$

where $f_Z = \frac{n_Z}{n_e}$ is the fraction of impurities.

Thus an eigenvalue equation for TE and ITG modes is obtained in the presence of impurities. Assuming a strongly ballooning eigenfunction with $k_{\parallel}^2 = (3q^2 R^2)^{-1}$,⁴¹ the eigenvalue equation is reduced to a system of algebraic equations that is solved numerically.

2.1.1 Impurity transport

The zero-flux impurity peaking factor (PF), defined as $PF = -\frac{RV_Z}{D_Z}$ for the value of the impurity density gradient that give zero impurity flux, is an important concept, as it quantifies the balance of convective and diffusive transport. Its derivation relies on the fact that the transport of a trace impurity species can locally be described by a diffusive and a convective part. In the trace impurity limit, i.e. for $Zf_Z \rightarrow 0$ in Eq. 6, the impurity flux Γ_Z becomes a linear function of ∇n_Z , offset by a convective velocity or “pinch” V_Z . The resulting expression can be seen in Eq. (7), where n_Z is the density of the impurity species and R is the major radius of the tokamak, and both the diffusion coefficient (D_Z) and the convective velocity (V_Z) are independent of ∇n_Z .⁸ Setting $\Gamma_Z = 0$ in Eq. (7) yields the interpretation of PF as the gradient of zero-impurity flux.

$$\Gamma_{n_Z} = -D_Z \nabla n_Z + n_Z V_Z \Leftrightarrow \frac{R\Gamma}{n_Z} = D_Z \frac{R}{L_{n_Z}} + RV_Z, \quad (7)$$

The relationship of PF to D_Z and V_Z is illustrated in Fig. 1.

The impurity particle flux at the left hand side of Eq. (7) can be written as:

$$\Gamma_{n_Z} = \langle \delta n_Z v_{\mathbf{E} \times \mathbf{B}} \rangle = -n_Z \rho_s c_s \left\langle \tilde{n}_Z \frac{1}{r} \frac{\partial \tilde{\phi}}{\partial \theta} \right\rangle. \quad (8)$$

The angled brackets imply a time and space average over all unstable modes. Performing this averaging for a fixed length scale $k_\theta \rho_s$ of the turbulence, the following expression is reached:

$$\begin{aligned} \frac{\Gamma_{n_Z}}{n_Z c_s} = \frac{k_\theta \rho_s \tilde{\gamma} |\tilde{\phi}_k|^2}{|N|^2} & \left\{ \frac{R}{2L_{n_Z}} \left(|\tilde{\omega}|^2 + \frac{14\tau_Z^*}{3} \tilde{\omega}_r + \frac{55\tau_Z^{*2}}{9} \right) - \right. \\ & \frac{R}{2L_{T_Z}} \left(2\tau_Z^* \tilde{\omega}_r + \frac{10\tau_Z^{*2}}{3} \right) - \langle \lambda \rangle \left(|\tilde{\omega}|^2 + \frac{10\tau_Z^*}{3} \tilde{\omega}_r + \frac{35\tau_Z^{*2}}{9} \right) + \\ & \left. \frac{Z}{3A_Z q_*^2 |N_1|^2} \left[\tau_Z^* \left(\frac{19}{3} \tilde{\omega}_r^2 - \frac{1}{3} \tilde{\gamma}^2 + \frac{100\tau_Z^*}{3} \tilde{\omega}_r - 5\tau_Z^{*2} \right) + 2\tilde{\omega}_r |\tilde{\omega}|^2 \right] \right\}, \quad (9) \end{aligned}$$

where $N_1 = \tilde{\omega} - 2\tau_Z^*$ is introduced.

In the following it is assumed that the turbulence is isotropic in the radial and poloidal directions (r and θ respectively; $k_r \rho_s = k_\theta \rho_s$), with a saturated fluctuation level of $|\phi_k| = \frac{\gamma}{\omega_{*e}} \frac{1}{k_\theta L_{n_e}}$.³² The first term in Eq. (9) corresponds to the diffusive part of Eq. (7), whereas the three subsequent terms correspond to the convective part of the transport. Of this, the R/L_{T_Z} term is the thermodiffusion, the sign of which is governed mainly by the real frequency, $\tilde{\omega}_r$. For TE modes, $\tilde{\omega}_r > 0$, and for ITG modes $\tilde{\omega}_r < 0$, resulting the thermodiffusion generally giving an inward pinch for TE modes and an outward pinch for ITG modes. Due to the Z -dependence in τ_Z^* , this term scales as $V_Z^{\nabla T} \sim 1/Z \cdot R/L_{T_Z}$ to leading order, rendering it unimportant for large Z impurity species, but it is important for lighter elements, such as the Helium ash. Further, the $\langle \lambda \rangle$ term gives the curvature pinch, which is usually inward, and the final term is the parallel compression term for the impurities. As opposed to the thermodiffusion, the parallel compression pinch is usually outward for TE modes and inward for ITG modes. Its Z dependence is $V_Z^{\parallel} \sim Z/A_Z k_{\parallel}^2 \sim Z/A_Z q^2$, but since $A_Z \approx 2Z$ this is expected to be a very weak scaling.⁸

2.2 Gyrokinetics – the GENE code

The GENE code⁴² is a massively parallel simulation code, solving the nonlinear time evolution of the gyrokinetic distribution functions on a fixed grid in phase space, i.e. an Eulerian approach. In GENE, the radial (x) and poloidal (y) dependencies are treated spectrally, i.e. those directions are discretised explicitly in k -space, whereas the toroidal (z) direction is discretised in real space.³¹

The simulation domain generally used in GENE is a so called flux tube. This is in essence a box that is elongated and twisted along with the \mathbf{B} field as field lines traverse the tokamak. An illustration of the result when the tube wraps up on itself can be seen in the cutaway presented in Fig. 3, where an area corresponding to a cross-section of the flux tube has been marked. There the size of the turbulent features can be seen, and a comparison of their size to the flux tube resolution of $\sim 125 \times 125$ ion gyro-radii supports the gyrokinetic approach.

The data presented in Fig. 3 is computed from the raw field data. By integrating further, scalar quantities can be obtained; those quantities are often the most interesting from a physics perspective, since they are easier to compare both to theoretical, experimental, and other numerical results. In this study, the scalar impurity flux Γ_Z is of most interest. Time series showing the fluctuations in the main ion density and the impurity flux for a nonlinear GENE simulation are presented in Fig. 2.

GENE can also be run in quasilinear mode, a method that is considerably less demanding when it comes computer resources, since the non-linear coupling between length scales is ignored.⁴³ This method only captures single unstable modes, not the interaction between dominant and sub-dominant modes, and only for the particular length scale $k_\theta \rho_s$ of choice. If the length scale is chosen appropriately, however, the quasilinear simulation will capture the essential features of the transport mechanism, and it is useful for getting a qualitative understanding of the physical processes.

3 Simulations

In this paper, the transport of impurities has been studied numerically, by calculating the impurity peaking factor (PF) for impurities of various Z and varying values of the driving background gradients. The process of calculating the peaking factor is illustrated in Fig. 1. The impurity particle flux Γ_Z is computed for ∇n_Z in the vicinity of $\Gamma_Z = 0$, taking the estimated uncertainty of the sample into account (see Fig. 2). The diffusivity D_Z and convective velocity RV_Z are then given by fitting the acquired fluxes to Eq. (7), whereafter the peaking factor is obtained as $PF = -\frac{RV_Z}{D_Z}$ (see section 2.1.1).

The instabilities causing the transport are fuelled by the free energy present in gradients in the system, and in general, the steeper the gradient the more free energy is available, which is expected to lead to stronger modes and more pronounced transport. Two families of gradients are available that can drive the instabilities: the temperature gradients $-R\nabla T_j/T_j \approx R/L_{T_j}$ and the density gradients $-R\nabla n_j/n_j \approx R/L_{n_j}$, where $j = i, e$ for main ions and electrons respectively.^{b)} Numerical studies have been performed, focused on the dependence of PF on these gradients.

The main parameters used in the simulations are summarised in Tab. I. The parameters were chosen to represent an arbitrary tokamak geometry at about mid radius, and do not represent any one particular experiment. As can be seen in the table, the choice between a TE and ITG mode dominated plasma was set by choosing a steep electron temperature gradient

^{b)}the density and temperature gradients of the impurity species can also drive turbulent transport, however, for trace amounts this effect is very small

($R/L_{T_w} = 7.0$) together with a moderate ion temperature gradient ($R/L_{T_i} = 3.0$) to prompt TE mode dominated dynamics, and the other way around for ITG mode dominance. It should be noted in this context, that TE modes can also be driven by steep density gradients. This case is omitted here, and left for future study.

For a typical NL simulation for main ions, fully kinetic electrons, and one trace species, a resolution of $n_x \times n_y \times n_z = 96 \times 96 \times 24$ grid points in real space and of $n_v \times n_\mu = 48 \times 12$ in velocity space was deemed sufficient. For QL GENE simulations the box size was set to $n_x \times n_y \times n_z = 8 \times 1 \times 24$ and $n_v \times n_\mu = 64 \times 12$ respectively.

Simulations have been performed with both deuterons and protons as main ions, but no significant differences were found between the two cases.

The impurities were included self-consistently as a third species in the simulations, with the impurity particle density $n_Z = 10^{-6}$ in order to ensure that they have a negligible effect on the turbulence.

4 Impurity peaking factors

4.1 Scalings with Z

For the Z scaling of PF , the charge number Z of the impurities was varied from $Z = 2$ to $Z = 74$ for the *TE* and *ITG* mode dominated cases.

QL and NL results were obtained using GENE and compared to results from the fluid model. The results are presented in Fig. 4(a) and Fig. 4(b) for the TE mode and the ITG mode case respectively. A good agreement between fluid and gyrokinetic results is observed, but notably the trends are more pronounced in the QL GENE results than in the QL fluid and NL GENE results. As expected from the discussion in section 2.1.1 above, PF varies the most for low Z impurities where the thermopinch is stronger. For heavier elements, the peaking factor saturates on levels well below neoclassical predictions, as seen in previous studies.^{1,8} The two cases show a qualitative difference, with PF falling towards saturation as Z is increased for the TE mode case, while the opposite holds for the ITG mode case.

The peaking factor comes close to zero for low Z in the ITG mode dominated case, however, the sign of PF remains positive for all Z in both the TE and the ITG mode dominated case. This indicates that a net inward flux is the general rule for all Z in both *TE* and *ITG* mode driven impurity transport.

The qualitative difference between the Z -scalings for the TE and ITG mode dominated cases can be understood from the balance of the thermodiffusion and parallel impurity compression in Eq. (9), the two terms having opposite signs for TE and ITG, as discussed above (section 2.1.1). The parallel impurity compression is almost independent of Z , so it can be assumed that the thermodiffusion is the main contributor to the observed trends. The thermodiffusion, on the other hand, has the strongest effect for low Z values, explaining the drop and rise of PF with Z for the TE and the ITG mode respectively. Since this term goes to zero for large values of Z , this also explains the observed saturation.

The difference between the QL and NL GENE results in Fig. 4(a) may be explained as a consequence of modifications of the linear mode structure through nonlinear effects. To investigate this, the fluid model was employed. In the fluid treatment, a strong ballooning eigenfunction is assumed with $k_{\parallel, sb}^2 = (3q^2 R^2)^{-1}$.⁴¹ Since the contribution from the parallel compression pinch depends on the mode structure along the field line, the results are expected to be sensitive to the choice of k_{\parallel} . A simplified treatment was used, varying k_{\parallel} around its strong ballooning value while keeping the eigenvalues fixed. The results are shown in Fig. 5 for $k_{\theta} \rho_s = 0.2$ and 0.3 in the TE and ITG mode dominated cases. As observed, the peaking factors for TE mode turbulence

is sensitive to the choice of k_{\parallel} , with the peaking factor going from $PF \approx 2$ to $PF \approx 0$ when k_{\parallel}^2 is varied from 0.5 to 2 times its strong ballooning value. The relative contribution of the parallel compression term to the convective flux will thus depend on k_{\parallel} , and as a consequence the scaling with Z will also be affected.

As is evident from Fig. 4, the value of PF is also dependent on the choice of $k_{\theta}\rho_s$, the perpendicular length scale. Finding the $k_{\theta}\rho_s$ that allows the QL models to best capture the behaviour of the transport is non-trivial. The nonlinear spectra for the fluctuations in the background electrostatic potential (ϕ) are illustrated in Fig. 6 for the TE and ITG mode dominated cases in Fig. 4.

The spectra both show a peak in the fluctuations at $k_{\theta}\rho_s \approx 0.15$, well below the wave number of maximum linear growth rate, $k_{\theta}\rho_s \approx 0.3$. We have confirmed that for $k_{\theta}\rho_s$ in the range 0.15–0.4, qualitatively similar QL results are obtained. In the following, $k_{\theta}\rho_s = 0.2$ –0.3 will be used.

A further complication that arises when studying TE mode turbulence is the onset of electron temperature gradient (ETG) driven modes. These are mostly sub-dominant, and so are not captured by the QL treatment, but may give a nonlinear contribution through the nonlinear coupling between the small scale ETG modes and the longer wave lengths of the dominant TE modes, and care has to be taken to avoid this effect.^{44,45}

4.2 Scalings with $\nabla T_{e,i}$

The scalings of the peaking factor with the temperature gradients were studied by varying $\nabla T_{e,i}$ for the TE and ITG mode regimes as defined above. QL results from GENE were compared to QL fluid results for three different species of impurities.

The resulting scalings of PF are presented in Fig. 7(a) for the TE case, and in Fig. 7(b) for the ITG case. Only weak trends were observed, in compliance with previous studies.^{13,17,40} As was observed for the Z -scaling in section 4.1 above, the trends for the TE and ITG mode dominated case are reversed; PF rises with driving gradient for the TE case, but falls for the ITG case.

The difference between the two trends can be partly understood from the thermodiffusion in Eq. (9). This term grows more important as the ion/impurity temperature gradient steepens, providing a strong outward pinch for the ITG mode dominated transport and thus lower values of PF as R/L_{T_z} increases (Fig. 7(b)). Since the impurity temperature gradient is constant for the ∇T_e scaling, however, other effects are behind the TE mode scaling in Fig. 7(a). The eigenvalues, in particular the mode growth rates, scale with $\nabla T_{e,i}$, as shown in Fig. 7(c). This will alter the relative contributions of the convective terms in Eq. 9, and hence a change in the peaking factor. We note here that the eigenvalues in Fig. 7(c) are normalised to c_s/R , giving $\omega_r < 0$ for TE modes and $\omega_r > 0$ for ITG modes.

As with the Z scaling, the sign of PF remains mostly positive for the $\nabla T_{e,i}$ scalings, though a modest flux reversal is observed when the trends of the scalings with Z and R/L_{T_i} for the ITG mode combine. This is the case for the He impurity in Fig. 7(b). The flux reversal happens only for very steep temperature gradients, however, so the conclusion is that the net impurity flux is generally inward regardless of the temperature gradient for both TE and ITG mode driven impurity transport.

4.3 Scaling with ∇n_e

For the TE and ITG mode cases considered, the electron density gradient was varied and the peaking factor calculated for a range of gradients. In order to preserve quasineutrality, Eq. (6),

$\nabla n_e = \nabla n_i$ was used.

The electron density gradient was varied over a broad range and QL trends were calculated from GENE data and contrasted with fluid results for impurity species of differing charge number Z . The estimated PF scalings for the TE and the ITG mode dominated case are shown in Fig. 8. The same trends are observed in both GENE and fluid data, with a strong sensitivity for lower Z impurities. This is particularly evident for the ITG mode case in Fig. 8(b), where the peaking factor for the He impurity shows a marked increase as ∇n_e steepens for both GENE and fluid results, whereas for the heavier elements a nearly flat dependence is observed. Qualitatively, the TE mode case and the ITG mode case are different from one another, the former showing the PF growing rapidly for flat gradients, but saturating at higher values, while for the latter the trend is more or less linear.

As shown in Fig. 8(c), the eigenvalues vary with the electron density gradient. A reduction of $|\omega_r|$ and an increase of γ are observed with increasing R/L_{n_e} , which leads to a reduction of the relative amplitude of the thermopinch in Eq. 9. This explains the observed PF scaling for the TE and ITG mode driven cases in Fig. 8(a) and Fig. 8(b) respectively.

As with the ∇T_i scaling, the combined effect of the Z and ∇n_e scalings is observed to lead to a flux reversal for the He impurity in the ITG mode dominated case in Fig. 8(b). This happens for flat electron density profiles in the QL GENE results. Outside of this regime the sign of PF remains positive, indicating a net inward impurity flux for both TE and ITG mode dominated impurity transport.

5 Conclusion and future work

In the present paper the transport of impurities by TE and ITG mode driven turbulence has been studied. Results obtained using a multi-fluid model were compared with quasilinear (QL) and nonlinear (NL) gyrokinetic results using the code GENE. The main part of the work was devoted to a comparison between TE mode and ITG mode dominated turbulence, with regard to the impurity peaking factor obtained for zero impurity flux. In particular, the scaling of the peaking factor with impurity charge Z and with the driving background gradients was investigated.

For the scaling with impurity charge Z , the TE and ITG mode dominated cases showed different scalings. For ITG mode driven impurity transport, the peaking factor was found to reach a minimum for low Z impurities. For larger Z values, the peaking factor was found to increase, followed by a saturation for $Z \gtrsim 20$ at a relatively low level, much below neoclassical predictions. The models considered (fluid and QL GENE) gave qualitatively similar results, in line with a previous study based on JET data¹ including NL GENE simulations. For TE driven transport, on the other hand, a rather flat Z scaling was obtained using fluid and NL GENE simulations, whereas the QL GENE simulations showed a slight increase of the peaking factor for low Z values. Hence, TE mode turbulence results in larger peaking factors than ITG mode turbulence for low Z values and vice versa for large Z impurities.

The difference in Z scalings are in line with the theoretical expectations based on the sign and Z -scaling of the different contributions to the convective impurity flux from the so called thermopinch and the parallel compression pinch (see discussion in section 2.1.1).

Using the fluid model it was shown that the peaking factors are quite sensitive to the mode structure along the field lines (k_{\parallel}) through the parallel compression pinch. Hence, the difference in scalings seen in QL GENE and NL GENE simulations may result from this effect (see discussion in section 4.1).

The scaling with the driving background gradients were in most cases found to be weak. The exception was the scaling with the density gradient for low Z values in ITG driven turbulence,

where a strong rising trend in PF with ∇n_e was observed.

It was found that the convective pinch is generally inward for both TE and ITG mode driven transport for all scalings.

The present study is based on low β plasmas in a simple s- α circular tokamak equilibrium. Future work will aim to study the effects of more realistic geometries, finite β , as well as effects of plasma rotation on impurity transport.

6 Acknowledgements

The simulations were performed on resources provided on the Lindgren⁴⁶ and HPC-FF⁴⁷ high performance computers, by the Swedish National Infrastructure for Computing (SNIC) at Paralleldatorcentrum (PDC) and the European Fusion Development Agreement (EFDA), respectively.

J. Vincent at PDC and T. Görler at IPP-Garching are acknowledged for their assistance concerning technical and implementational aspects in making the GENE code run on the PDC Lindgren super-computer.

A. Strand and L. Strand at Herrgårdsskolan are acknowledged for their help with the nonlinear simulations.

The authors would also like to thank F. Jenko, M. J. Püschel, F. Merz and the rest of the GENE team at IPP-Garching for their valuable support and input.

References

- [1] H. Nordman, A. Skyman, P. Strand, C. Giroud, F. Jenko, and F. Merz et al. Fluid and gyrokinetic simulations of impurity transport at JET. *On JET-pinboard (EFDA-JET-PR(10)51)*; Submitted to *Plasma Phys. Contr. F.*, 2011.
- [2] M. Fröjd, M. Liljeström, and H. Nordman. Impurity effects on η_i mode stability and transport. *Nucl. Fusion*, 32(3):419, Mar. 1992.
- [3] R. Basu, T. Jessen, V. Naulin, and J. Juul Rasmussen. Turbulent flux and the diffusion of passive tracers in electrostatic turbulence. *Phys. Plasmas*, 10(7):2696, Mar. 2003.
- [4] T. Dannert and F. Jenko. Gyrokinetic simulation of collisionless trapped-electron mode turbulence. *Phys. Plasmas*, 12(7):072309, July 2005.
- [5] C. Estrada-Mila, J. Candy, and R.W. Waltz. Gyrokinetic simulations of ion and impurity transport. *Phys. Plasmas*, 12(2):022305, Jan. 2005.
- [6] V. Naulin. Impurity and trace tritium transport in tokamak edge turbulence. *Phys. Rev. E*, 71(1):015402, Jan. 2005.
- [7] M. Priego, O. E. Garcia, V. Naulin, and J. Juul Rasmussen. Anomalous diffusion, clustering, and pinch of impurities in plasma edge turbulence. *Phys. Plasmas*, 12(6):062312, June 2005.
- [8] C. Angioni and A. G. Peeters. Direction of impurity pinch and auxiliary heating in tokamak plasmas. *Phys. Rev. Lett.*, 96:095003, Mar. 2006.
- [9] T. Fülöp and J. Weiland. Impurity transport in ITER-like plasmas. *Phys. Plasmas*, 13(11):112504, Nov. 2006.
- [10] C. Angioni et al. Particle and impurity transport in the Axial Symmetric Divertor Experiment Upgrade and the Joint European Torus, experimental observations and theoretical understanding. *Phys. Plasmas*, 14(5):055905, Apr. 2007.
- [11] C. Bourdelle, X. Garbet, F. Imbeaux, A. Casati, N. Dubuit, R. Guirlet, and T. Parisot. A new gyrokinetic quasilinear transport model applied to particle transport in tokamak plasmas. *Phys. Plasmas*, 14(11):112501, Nov. 2007.
- [12] N. Dubuit, X. Garbet, T. Parisot, R. Guirlet, and C. Bourdelle. Fluid simulations of turbulent impurity transport. *Phys. Plasmas*, 14(4):042301, Apr. 2007.
- [13] H. Nordman, T. Fülöp, J. Candy, P. Strand, and J. Weiland. Influence of magnetic shear on impurity transport. *Phys. Plasmas*, 14(5):052303, May 2007.
- [14] H. Nordman, R. Singh, and T. Fülöp et al. Influence of the radio frequency ponderomotive force on anomalous impurity transport in tokamaks. *Phys. Plasmas*, 15:042316, 2008.
- [15] C. Angioni, A. G. Peeters, G. V. Pereverzev, A. Bottino, J. Candy, R. Dux, E. Fable, T. Hein, and R. E. Waltz. Gyrokinetic simulations of impurity, helium and α particle transport and consequences on ITER transport modelling. *Nucl. Fusion*, 49(5):055013, May 2009.
- [16] Y. Camenen, A. G. Peeters, C. Angioni, F. J. Casson, W. A. Hornsby, A. P. Snodin, and D. Strintzi. Impact of the background toroidal rotation on particle and heat turbulent transport in tokamak plasmas. *Phys. Plasmas*, 16(1):012503, Jan. 2009.

- [17] T. Fülöp and H. Nordman. Turbulent and neoclassical impurity transport in tokamak plasmas. *Phys. Plasmas*, 16(3):032306, Mar. 2009.
- [18] T. Fülöp, S. Braun, and I. Pusztai. Impurity transport driven by ion temperature gradient turbulence in tokamak plasmas. *Phys. Plasmas*, 17(6):062501, July 2010.
- [19] S. Futatani, X. Garbet, S. Benkadda, and N. Dubuit. Reversal of impurity pinch velocity in tokamak plasma with a reversed magnetic shear configuration. *Phys. Rev. Lett.*, 104(1):015003, Jan. 2010.
- [20] T. Hein and C. Angioni. Electromagnetic effects on trace impurity transport in tokamak plasmas. *Phys. Plasmas*, 17(1):012307, Jan. 2010.
- [21] S. Moradi, M. Z. Tokar, and B. Weyssow. Modeling of impurity effect on drift instabilities in plasmas with many ion species. *Phys. Plasmas*, 17(1):012101, Jan. 2010.
- [22] T. Fülöp and S. Moradi. Effect of poloidal asymmetry on the impurity density profile in tokamak plasmas. *Phys. Plasmas*, 18(3):030703, Feb. 2011.
- [23] R. Dux, R. Neu, A. G. Peeters, G. Pereverzev, A. Mück, F. Ryter, and J. Stober. Influence of the heating profile on impurity transport in ASDEX Upgrade. *Plasma Phys. Contr. F.*, 45(9):1815, Sep. 2003.
- [24] M. E. Puiatti, M. Valisa, and M. Mattioli, et al. Simulation of the time behaviour of impurities in JET Ar-seeded discharges and its relation with sawtooth and RF heating. *Plasma Phys. Contr. F.*, 45(12):2011, Dec. 2003.
- [25] M. E. Puiatti, M. Valisa, and C. Angioni, et al. Analysis of metallic impurity density profiles in low collisionality Joint European Torus H-mode and L-mode plasmas. *Phys. Plasmas*, 13(4):042501, Apr. 2006.
- [26] C. Giroud, R. Barnsley, and P. Buratti, et al. Method for experimental determination of Z dependence of impurity transport on JET. *Nucl. Fusion*, 47(4):313, Apr. 2007.
- [27] C. Giroud et al. 12th international workshop on “H-mode physics and transport barriers”, Sep. 30–Oct. 2 2009. Princeton, USA.
- [28] P. Helander and D. J. Digmars. *Collisional Transport in Magnetized Plasmas*. Cambridge University Press, 2002.
- [29] F. Jenko, W. Dorland, M. Kotschenreuther, and B. N. Rogers. Electron temperature gradient driven turbulence. *Phys. Plasmas*, 7(5):1904, May 2000.
- [30] T. Dannert. *Gyrokinetische Simulation von Plasmaturbulenz mit gefangenen Teilchen und elektromagnetischen Effekten*. Ph.d. thesis (monography), Technischen Universität München, 2005.
- [31] F. Merz. *Gyrokinetic Simulation of Multimode Plasma Turbulence*. Ph.d. thesis (monography), Westfälischen Wilhelms-Universität Münster, 2008.
- [32] J. Weiland. *Collective Modes in Inhomogeneous Plasmas*. IoP Publishing, 2000.
- [33] T. M. Antonsen and B. Lane. Kinetic equations for low frequency instabilities in inhomogeneous plasmas. *Phys. Fluids*, 23(6):1205, June 1980.

- [34] E. A. Frieman and L. Chen. Nonlinear gyrokinetic equations for low-frequency electromagnetic waves in general plasma equilibria. *Phys. Fluids*, 25(3):502, Mar. 1982.
- [35] T. S. Hahm, W. W. Lee, and A. Brizard. Nonlinear gyrokinetic theory for finite-beta plasmas. *Phys. Fluids*, 31(7):1940, July 1988.
- [36] A. Brizard. Nonlinear gyrokinetic Maxwell-Vlasov equations using magnetic co-ordinates. *J. Plasma Phys.*, 41(3):541, June 1989.
- [37] R. D. Hazeltine and J. D. Meiss. *Plasma Confinement*. Dover Publications, 2003.
- [38] J. Anderson, H. Nordman, and J. Weiland. Effects of non-circular tokamak geometry on ion-temperature-gradient driven modes. *Plasma Phys. Contr. F.*, 42(5):545, May 2000.
- [39] J. Anderson, T. Rafiq, M. Nadeem, and M. Persson. A comparison of drift wave stability in stellarator and tokamak geometry. *Phys. Plasmas*, 9(5):1629, May 2002.
- [40] H. Nordman, P. Strand, and X. Garbet. Collisionless trapped-electron-mode turbulence and transport in fluid descriptions. *J. Plasma Phys.*, 73(5):731–740, 2007.
- [41] A. Hirose, L. Zhang, and E. Elia. Higher order collisionless ballooning mode in tokamaks. *Phys. Rev. Lett.*, 72(25):3993–3996, June 1994.
- [42] The GENE code, 14 Jan 2011. <http://www.ipp.mpg.de/~fsj/gene/>.
- [43] F. Merz and F. Jenko. Nonlinear saturation of trapped electron modes via perpendicular particle diffusion. *Phys. Rev. Lett.*, 100(3):035005, Jan. 2008.
- [44] D. R. Ernst, J. Lang, W. M. Nevins, M. Hoffman, and Y. Chen. Role of zonal flow in trapped electron mode turbulence through nonlinear gyrokinetic particle and continuum simulation. *Phys. Plasmas*, 16(5):055906, May 2009.
- [45] Z. Gao, H. Sanuki, K. Itoh, and J. Q. Dong. Short wavelength electron temperature gradient instability in toroidal plasmas. *Phys. Plasmas*, 12(2):022503, Jan. 2005.
- [46] Lindgren. <http://www.pdc.kth.se/resources/computers/lindgren/>.
- [47] HPC-FF. <http://www2.fz-juelich.de/jsc/juropa/>.

TAB. I: Parameters used in the gyrokinetic simulations, [†] denotes scan parameters

	ITG:	TE:
T_i/T_e :	1.0	1.0
s :	0.8	0.8
q :	1.4	1.4
$\varepsilon = r/R$:	0.14	0.14
$n_e, n_i + n_Z$:	1.0	1.0
n_Z (<i>trace</i>):	10^{-6}	10^{-6}
$R/L_{n_{i,e}}$: [†]	2.0–3.0	2.0–3.0
$R/L_{T_i}, R/L_{T_Z}$: [†]	7.0	3.0
R/L_{T_e} : [†]	3.0	7.0

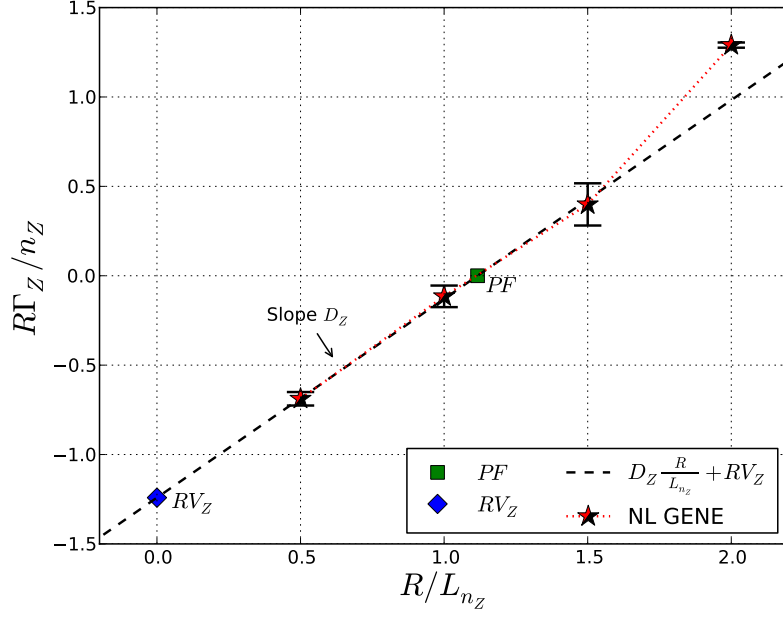


FIG. 1: Impurity flux (Γ_Z) dependence on the impurity density gradient ($-R\nabla n_Z/n_Z = R/L_{n_Z}$), illustrating the peaking factor (PF), the diffusivity (D_Z) and pinch (RV_Z), and the validity of the linearity assumption in Eq. (7) of $\Gamma_Z|_{\nabla n_Z \approx 0}$ for trace impurities. Parameters of Eq. (7) are estimated from the three samples closest to zero impurity flux ($\Gamma_Z = 0$), taking the estimated error of the data into account. The flux is acquired as the average of a time series after convergence, as is illustrated in Fig. 2. Data from NL GENE simulations of TE mode driven turbulence with He impurities and parameters as in Fig. 4(a). The error bars indicate an estimated error of one standard deviation.

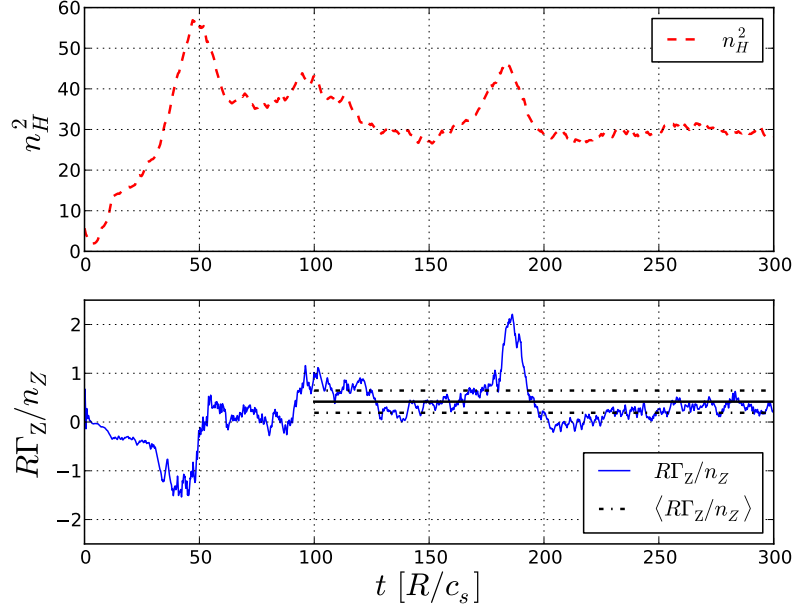


FIG. 2: Time series showing fluctuations in the main ion density (n_H^2) and impurity flux (Γ_z) after averaging over the whole flux tube (see Fig. 3). The averaged impurity flux ($\langle \Gamma_Z \rangle$) is calculated from Γ_Z , discarding the first portion to ensure that the linear phase of the simulation is not included. $\langle \Gamma_Z \rangle$ is used for finding the peaking factor for the impurity species, as is illustrated in Fig. 1. The bursty nature of the transport is seen in the peak around $t \approx 185 R/c_s$. These bursts have been found to affect the average flux little, but to significantly increase the estimated error in $\langle \Gamma_Z \rangle$ ($-\cdot-$). Data from NL GENE simulation of TE mode driven turbulence with He impurities. The parameters are the same as in Fig. 4(a), with $-R\nabla n_Z/n_Z = R/L_{n_Z} = 1.5$.

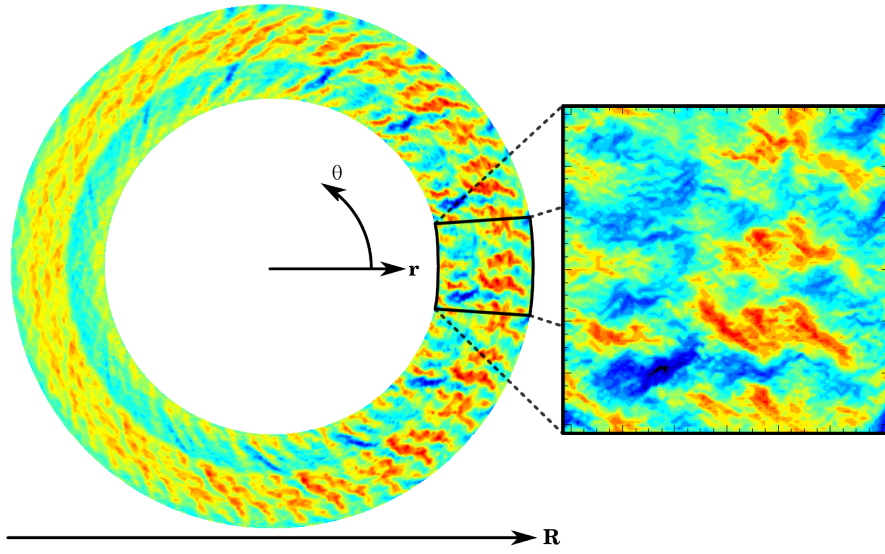
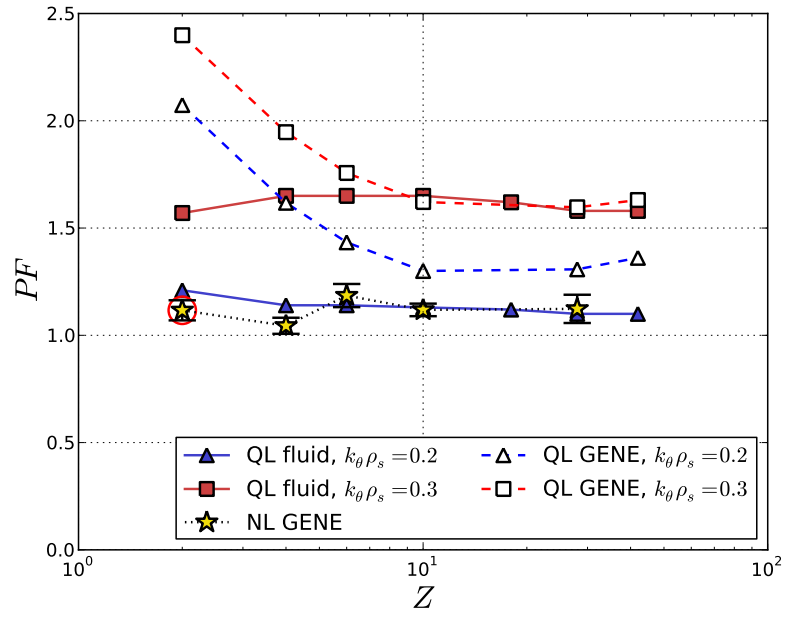
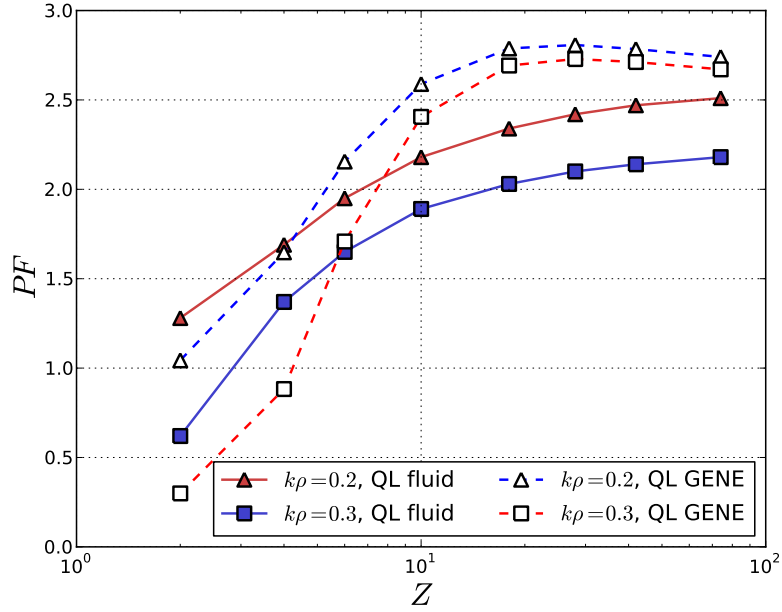


FIG. 3: A cut from the toroidal annulus made up of the flux tube as it twists around the torus following the \mathbf{B} field, showing the fluctuation of the electrostatic potential ϕ . The marked area corresponds to a cross-section of the flux tube. Data from NL GENE simulation of TE mode turbulence, with parameters as in Fig. 4(a) at $t \approx 300 R/c_s$.



4(a): dependence of the peaking factor (PF) on Z for the TE case



4(b): dependence of the peaking factor (PF) on Z for the ITG case

FIG. 4: Scalings of the peaking factor (PF) with impurity charge (Z). Parameters are $q = 1.4$, $s = 0.8$, $\varepsilon = r/R = 0.143$ in both subfigures, with $R/L_{T_i} = R/L_{T_z} = 3.0$, $R/L_{T_e} = 7.0$, $R/L_{n_e} = 2.0$ for the TE case (Fig. 4(a)), and $R/L_{T_i} = R/L_{T_z} = 7.0$, $R/L_{T_e} = 3.0$, $R/L_{n_e} = 3.0$ for the ITG case (Fig. 4(b)). The error bars for the NL GENE results in Fig. 4(a) indicate an estimated error of one standard deviation. The sample for the He impurity acquired from the data illustrated in Fig. 1 and Fig. 2 is highlighted (\circ).

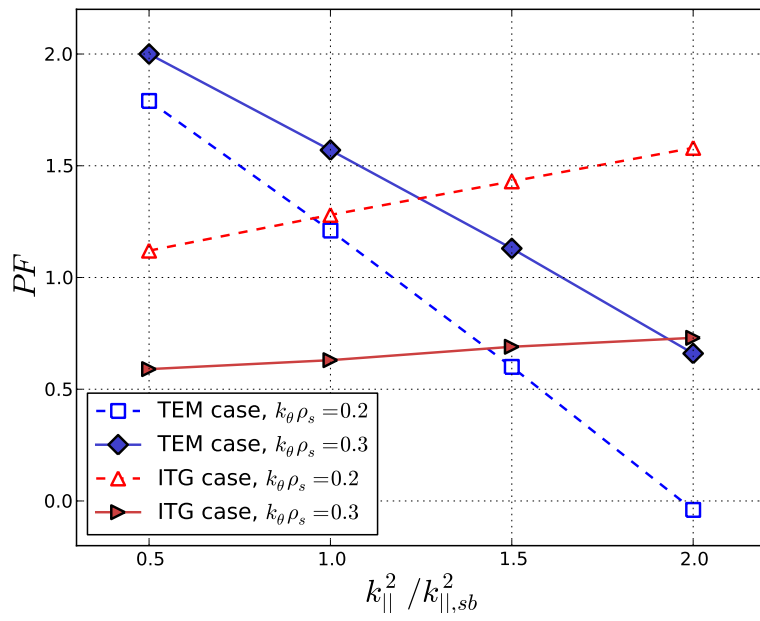


FIG. 5: Scaling of the peaking factor (PF) with $k_{||}^2/k_{||,sb}^2$ for He impurity, where $k_{||,sb}^2 = (3q^2R^2)^{-1}$ is the strong ballooning value;⁴¹ QL fluid results with parameters as in Fig. 4(a) (TE) and Fig. 4(b) (ITG).

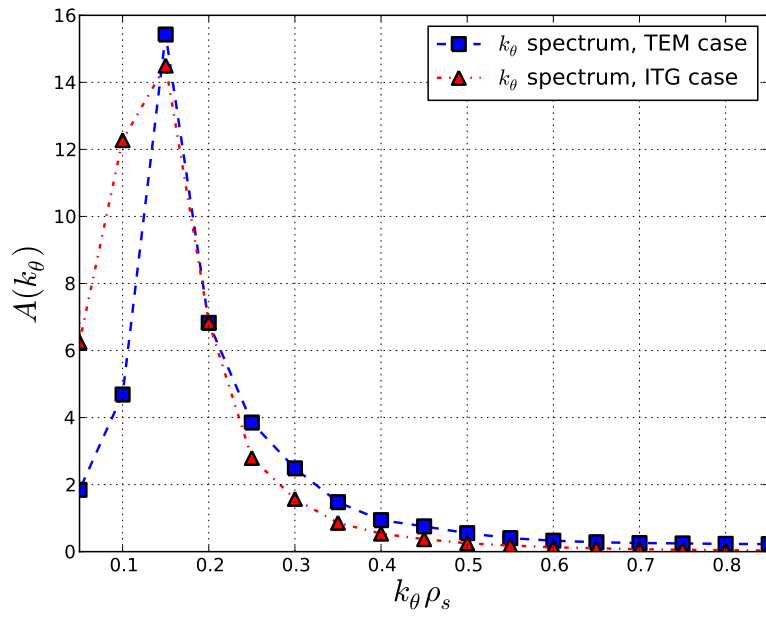
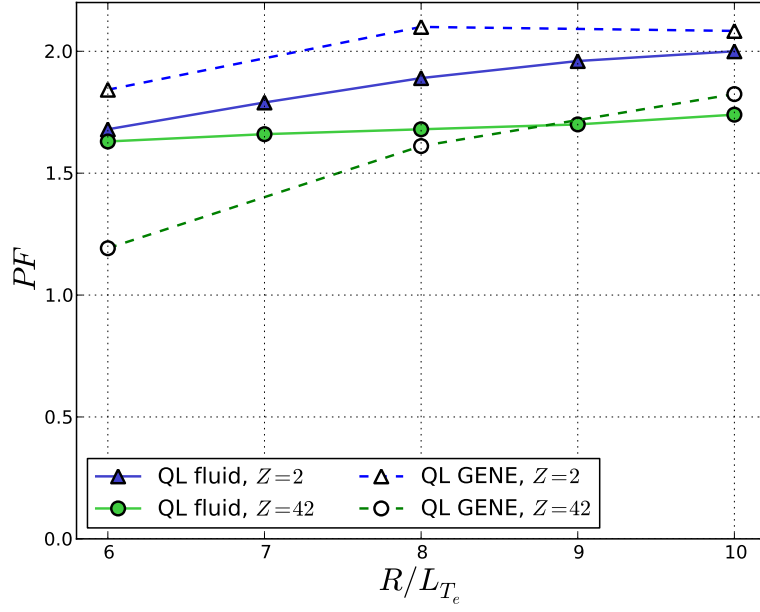
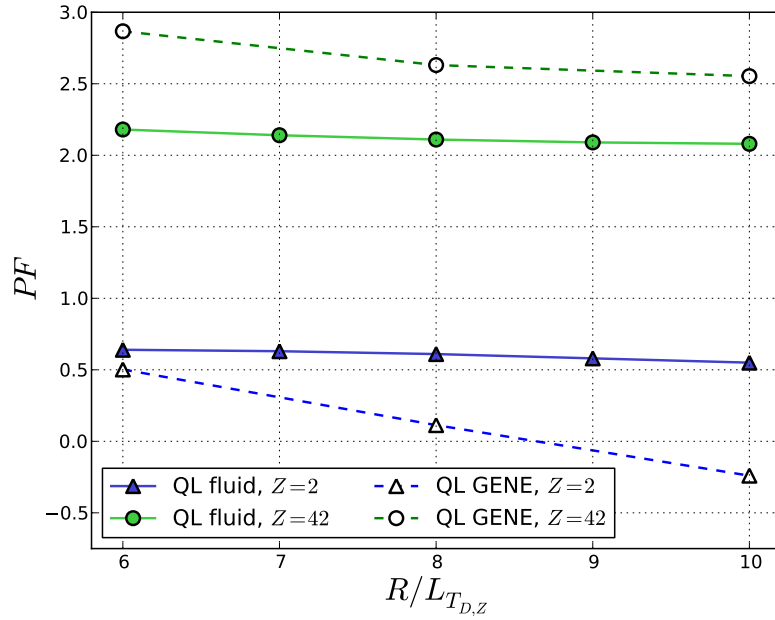


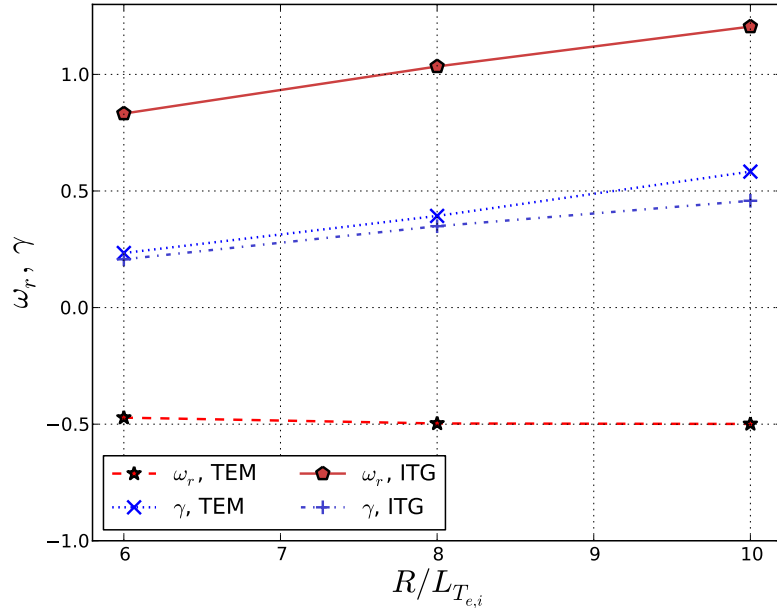
FIG. 6: Spectra showing the normalised amplitude ($A(k_\theta \rho_s)$) of the fluctuations in the background electrostatic potential (ϕ) as a function of $k_\theta \rho_s$; NL GENE results with parameters as in Fig. 4(a) (TE) and Fig. 4(b) (ITG).



7(a): dependence of the peaking factor (PF) on the normalised electron temperature gradient for the TE case

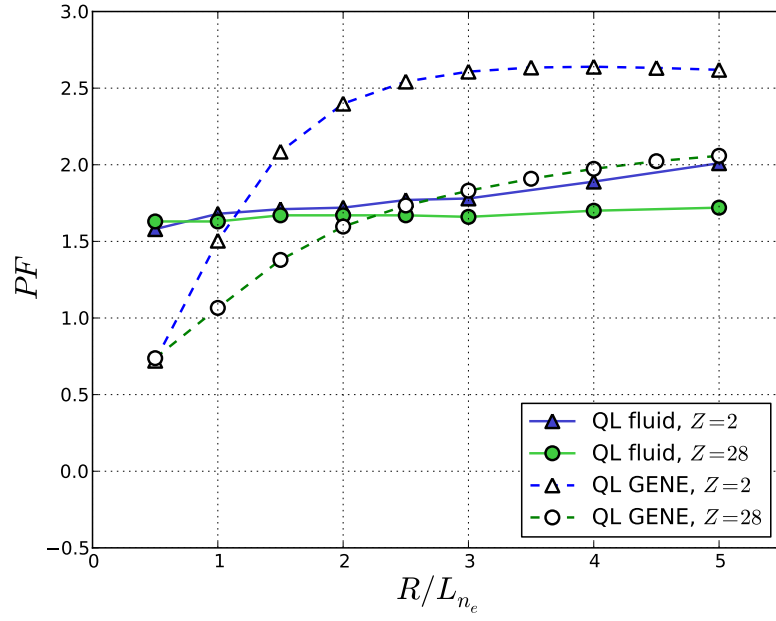


7(b): dependence of the peaking factor (PF) on the normalised ion temperature gradient for the ITG case;

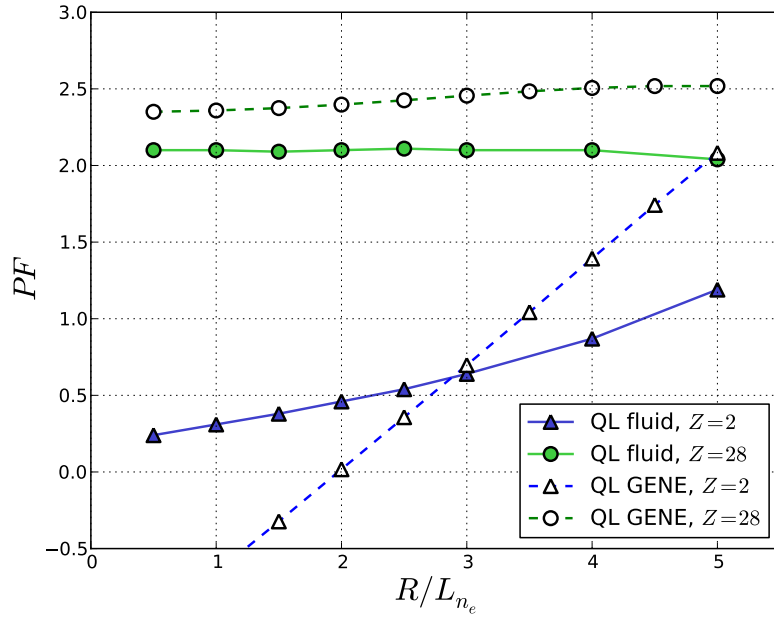


7(c): real frequency (ω_r) and growth rate (γ) for the two cases in Fig. 7(a) and Fig. 7(b)

FIG. 7: Scalings of the peaking factor (PF) with the electron and ion temperature gradients ($-R\nabla T_{e,i}/T_{e,i} = R/L_{T_{e,i}}$). Parameters for the TE and ITG mode case as in Fig. 4, with $R/L_{n_e} = 3.0$ and $k_\theta \rho_s = 0.3$ for both cases. The eigenvalues in Fig. 7(c) are from QL GENE simulations, they are normalised to c_s/R .

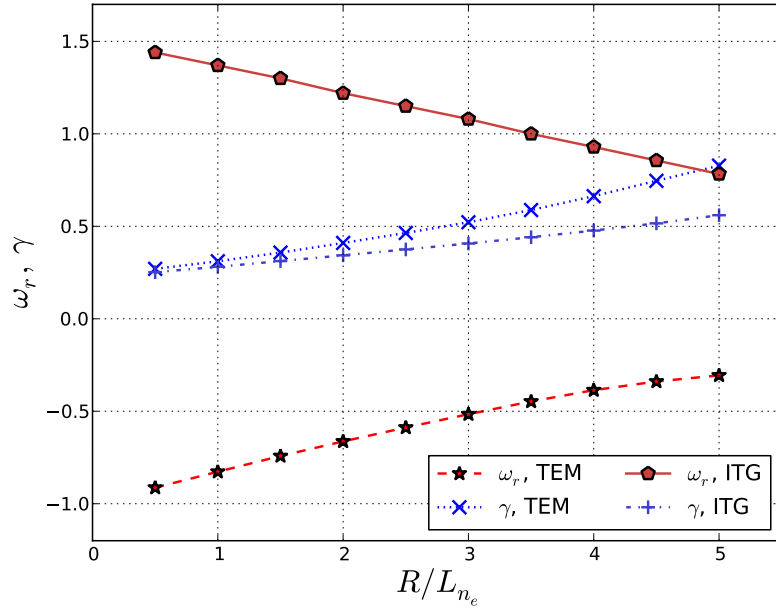


8(a): dependence of the peaking factor (PF) on the normalised electron density gradient for the TE case



8(b): dependence of the peaking factor (PF) on the normalised electron density gradient for the ITG case

4



8(c): real frequency (ω_r) and growth rate (γ) for the two cases in Fig. 8(a) and Fig. 8(b)

FIG. 8: Scalings of the peaking factor (PF) with the electron density gradient ($-R\nabla n_e/n_e = R/L_{n_e}$). Parameters for the TE and ITG mode cases as in Fig. 4, with $k_\theta \rho_s = 0.3$ for both cases. The eigenvalues in Fig. 8(c) are from QL GENE simulations, they are normalised to c_s/R .